INORGANIC CHEMISTRY FRONTIERS

RESEARCH ARTICLE

View Article Online
View Journal | View Issue

Cite this: *Inorg. Chem. Front.*, 2023, **10**, 2457

Hierarchical Cu-MOF hollow nanowire modified copper mesh for efficient antibacterial PM filtration†

Haiyan Li,[a] Tao Wang,*[a] Yulong Ying,[a] Zhiqi Wang,[a] Lianjun Pan[b] and Sheng Wang*[a]

Received 23rd February 2023,
Accepted 16th March 2023

DOI: 10.1039/d3qi00349c

rsc.li/frontiers-inorganic

The filtration of fine particulate matter (PM) particles poses a significant threat to public health, with potentially adverse effects on the lungs and blood. Metal mesh filters have shown potential as multifunctional PM filters; however, filtration of fine PM particles is still challenging. In this study, we developed a hierarchical metal–organic-framework-based structure (Cu-MOF hollow nanowires) on copper mesh for PM filtration. The *in situ* grown three-dimensional (3D) Cu-MOF hollow nanowires effectively reduced the pore size and provided an enhanced electrostatic surface with maximum MOF exposure. This Cu-MOF coated metal mesh demonstrated excellent filtration efficiencies in a small-size PM regime (89.1% for PM0.3, 90.4% for PM0.5, 93.8% for PM1.0, and 98.1% for PM2.5). Furthermore, the filter exhibited excellent antibacterial performance against both *S. aureus* and *E. coli*. These attractive metal-based materials show potential in developing energy-saving and high-efficient metal-based filters for various applications.

1. Introduction

Air pollution caused by particulate matter (PM) is a significant environmental issue that seriously threatens human health.[1–3] Generally, PM particles are classified into three types based on their aerodynamic equivalent diameter (AED): coarse, fine, and ultrafine particles (AED > 2.5 μm, AED = 0.1–2.5 μm, and AED < 0.1 μm, respectively).[4] Among these particles, fine particles are particularly hazardous as they tend to carry toxic organics, heavy metals, and harmful microorganisms due to their higher specific surface area and active adsorption sites.[5] Therefore, there is a pressing need to design an advanced filter that combines high fine PM removal efficiency with bacterial inhibition properties.

According to classical filtration theory, the filtration mechanism can be either passive or proactive, depending on the interaction between the filter materials and PM particles.[6–8] In the passive process, the primary mechanism is structure-based filtration, where the filter materials act as an "obstacle" to the particle-transport path and achieve filtration through physical collision, attachment, and trapping. In contrast, interaction-based filtration, *i.e.*, the chemical and electrostatic interactions between PM particles and filter materials, becomes dominant in the proactive process. Most fiber-based filters are designed based on the passive trapping mechanism, *i.e.*, blocking off the contaminants. While nanofiber-based air filters have been proven to be superior to microfibers in various aspects,[9] the clogging effect has significantly shortened their lifetime due to their narrow pore structures.[10,11]

In a proactive filtration method, electrostatic precipitation and centrifugal collection are the most common ways to remove PMs. However, these methods require large energy consumption and take up large volume space. Recently, researchers have realized that surface modification of high-polarity materials in the filter can remarkably enhance the electrostatic interactions and improve the filtration efficiency.[12,13] Corona charging or tribocharging of electret nanofibrous membranes using high-polarity polymer materials can efficiently capture PMs.[14] Nylon-6 and poly(vinylidene fluoride) (PVDF) are representative high-polarity polymer materials with a high dipole moment.[15,16] Gu *et al.* developed a high-efficiency rotating TENG (R-TENG)-enhanced PI-nanofiber air filter for PM removal under an ambient atmosphere, around which an electric field was formed and led to a significantly improved removal efficiency.[17] However, achieving the charge stability of electret materials for air filtration is still a big challenge.[14]

Metal–organic frameworks (MOFs) have recently attracted great attention because of their ultrahigh porosity, high thermal and chemical stability, and abundant

[a]*School of Materials Science and Engineering, Zhejiang Sci-Tech University, Hangzhou 310018, China. E-mail: wangtao@zstu.edu.com, taotao571@hotmail.com, wangsheng@zstu.edu.com, wangsheng571@hotmail.com*
[b]*Zhejiang Light Industrial Products Inspection and Research Institute, Hangzhou 310000, China*

† Electronic supplementary information (ESI) available. See DOI: https://doi.org/10.1039/d3qi00349c

functionalities.[18–21] The pioneering work of Wang *et al.* has led to a series of follow-up studies on the incorporation of MOFs into filtration systems for enhanced PM capture *via* electrostatic forces.[22–24] However, the exposure degree of MOFs remains challenging due to the limited loading process.[22,24] To date, loading MOFs on substrates has mainly included *in situ* growth,[25,26] mechanical loading,[27,28] binder-assistant binding,[29,30] and electrospinning.[31,32] *In situ* growth is the most convenient method, but most supports are chemically inert and not suitable for loading. Severe agglomeration of MOFs often occurs during the operation of mechanical loading. Adding binders can improve the loading and robustness of the MOF coating, but both the porosity and active sites will be significantly reduced.[29] The application of the electrospinning method often results in MOF nanocrystals being wrapped into nanofibers. As such, achieving appropriate bonding between highly effective MOFs and the substrate is crucial to realizing high filtration efficiency, longevity, reusability, and low cost.

Metal mesh filters are widely used in the industry due to their excellent durability and reliability.[33,34] However, their filtration precision and performance on fine particles remain relatively low. Typically, electric or magnetic devices are necessary to aid in capturing fine PMs with metal filters, but this consumes high levels of energy.[35] Few reports have been published thus far on metal mesh filters capable of filtering fine PMs without energy consumption.[36] Given that MOFs can form and grow directly on the mesh surface, we introduce a novel self-sacrificial template strategy in this work to fabricate a PM filter utilizing 3D Cu-MOF hollow nanowires (NWs) on a commercial copper mesh. The physical PM screening of hierarchically structured and electrostatic PM screening of the partially charged surface of Cu-MOFs played critical roles in improving air filter properties. Furthermore, the composite mesh filter exhibited impressive antibacterial performance. In contrast to previous metal mesh filters, our work provides insight into the production of efficient antibacterial PM filters based on metal meshes. This approach can effectively protect individuals from the threat posed by pathogenic aerosols and airborne PM.

2. Experimental

2.1. Materials

2,3,6,7,10,11-Hexahydroxytriphenylene (HHTP, 95%) and ammonium persulfate ($(NH_4)_2S_2O_8$, 98%) were acquired from Macklin Biochemical Co., Ltd. Copper mesh (400 mesh size) was purchased from Changzhou Sa Small wire Mesh Co., Ltd. *N*,*N*-Dimethylformamide (DMF, 99%) was supplied by Hangzhou Shuanglin Chemical Reagent Co., Ltd. All chemicals and solvents were of analytical grade and used as received without further purification.

2.2. Methods

2.2.1. Preparation of $Cu(OH)_2$ covered copper mesh (CHM). The commercial copper mesh was sequentially cleaned with acetone, ethanol, distilled water, and 1 M HCl to remove impurities and oxides. Then, the cleaned copper mesh was immersed in a mixed aqueous solution of 2 M NaOH and 0.1 M $(NH_4)_2S_2O_8$ for 20 min. Subsequently, the obtained mesh was treated with distilled water and dried in an oven. The resulting mesh was named CHM.

2.2.2. Preparation of Cu-MOF covered copper mesh (CMM). The as-prepared CHM was first immersed in a mixture of 80 mL distilled water and 8 mL DMF solution. Then 30 mg HHTP was added into the solution and kept in a preheated oven at a certain temperature for 10 min. Finally, the resulting mesh was washed with distilled water and dried in an oven. After naturally cooling down to room temperature, the resulting sample was thoroughly rinsed with acetone and used for future characterization and applications. The entire synthetic process was fast and facile.

Here, the resultant modified meshes obtained at different temperatures were named "CMM-T", where T denotes the specific reaction temperature (30, 50, 70, and 90 °C) used for the growth of MOFs.

2.2.3. PM filtration performance evaluation. An automated filtration system (LZC-K, Suzhou Huada Instrument Equipment Co., Ltd, China) was used to evaluate the filtration performance in all size regimes. Charge-neutralized NaCl aerosol particles (300 000–500 000), with a mass mean diameter of 0.3–10 μm, were delivered through the filter (an effective area of 100 cm^2). All test conditions strictly followed the international standards. The filtration test was repeated three times for each test filter.

The filtration efficiency (E) could be calculated from the PM particle concentration between upstream (C_0) and downstream (C) using eqn (1). The pressure drop (ΔP) was obtained from the pressure difference between upstream (P_1) and downstream (P_2) using eqn (2). The quality factor (Q_f) could be calculated using eqn (3).

$$E=(C_0 - C)/C_0 \times 100\% \quad (1)$$

$$\Delta P = P_1 - P_2 \quad (2)$$

$$Q_f=\frac{-\ln(1-E)}{\Delta P} \quad (3)$$

2.2.4. Evaluation of antibacterial properties. Plate counting method analyses were conducted to evaluate the antibacterial properties of the mesh filters.[37] The Gram-positive bacterium *Staphylococcus aureus* (*S. aureus*, ATCC 6538) and Gram-negative bacterium *Escherichia coli* (*E. coli*, ATCC 25922) were used in this study. The final concentrations of *S. aureus* and *E. coli* were determined to be 2.39×10^7 and 1.5×10^7 CFU mL^{-1}, respectively.

2.3. Characterization

The structure and surface morphology of the filter sample were examined with a field emission scanning electron microscope (FESEM, ZEISS VLTRA-55, Germany) and transmission electron microscope using a JEOL instrument (TEM, JEM-2010

HR) operated at 200 kV. The composition of the mesh sample was studied using energy-dispersive X-ray analysis (EDX, IncaEnergy-200). Fourier-transform infrared (FT-IR) spectrum of the mesh sample were recorded using a Nicolet 5700 FT-IR spectrometer. The crystalline structure of the mesh sample was analyzed by X-ray diffraction (XRD) measurements (Rigaku D/max-2200 diffractometer employing Cu-Kα radiation (λ = 0.154 nm)). The scanning rate was 2° min^{-1} at 2θ angles from 3° to 80°. X-ray photoelectron spectroscopy (XPS, Thermo Scientific K-Alpha) with a monochromatized Al-Kα X-ray source operated at 12 kV and 20 mA was applied for elemental analysis. N_2 adsorption and desorption analyses of the mesh sample were performed on a nitrogen adsorption analyzer (BeiShiDe 3H-2000BET-A, China).

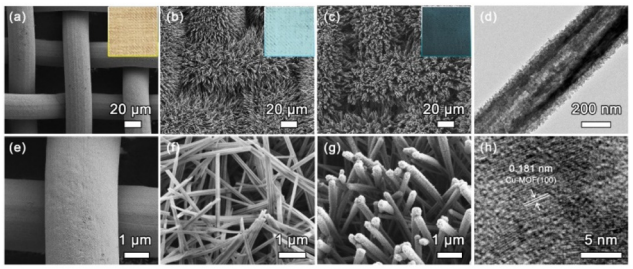

Fig. 1 Morphology characterization. (a and e) SEM images of the pristine copper mesh. Top view and magnified SEM images of (b and f) CHM and (c and g) CMM. (d) TEM and (h) HRTEM images of individual Cu-MOF hollow structures. The insets in figure a–c show the corresponding photographs of copper mesh, CHM, and CMM.

3. Results and discussion

3.1. Characterization of Cu-MOF covered copper mesh

The self-sacrificial template strategy for preparing the Cu-MOF covered metal mesh filter is presented in Scheme 1. It involves two straightforward steps: the *in situ* growth of $Cu(OH)_2$ NW arrays on the copper mesh (CHM), followed by the *in situ* transformation of $Cu(OH)_2$ NWs to Cu-MOF hollow structures (CMM).[38–40] The $Cu(OH)_2$ NWs act as self-sacrificial templates and deprotonating agents. The CMM formation process can be explained by the Kirkendall effect, which is a widely used method to construct micro/nano-hollow structures *via* the diffusion rate difference of two ion species.[41–43]

First, the morphologies of the copper mesh, CHM, and CMM were characterized by scanning electron microscopy (SEM) (for EDX spectra, see Fig. S2a–c†). The pristine copper mesh consisted of interwoven smooth copper microwires with a diameter of approximately 25 μm, exhibiting a net-like structure with a pore diameter of 40 μm (Fig. 1a and e). After the oxidation process, large amounts of $Cu(OH)_2$ NWs, with a length of around 10 μm and a diameter of approximately 200–500 nm, grew on the surfaces of Cu wires, forming numerous micro/nano-scale bark-like grooves and filling the empty spaces of the copper mesh (Fig. 1b and f). The resulting CHM showed a pale blue appearance, suggesting the formation of $Cu(OH)_2$ (inset in Fig. 1b).

Then, the CHM was immersed in HHTP solution, and the color of the mesh quickly turned black-green. The SEM images clearly showed the rough coral branch-like structure of the obtained Cu-MOF, with a larger diameter of 400–600 nm than that of the $Cu(OH)_2$ NWs (Fig. 1c and g), led to a further space decrease in the copper mesh. The transmission electron microscopy (TEM) image revealed that the Cu-MOF has a hollow structure containing many intergrown nanoparticles of approximately 20–40 nm (Fig. 1d). The tubular-shaped NWs with a well-defined hollow interior were also distinguishable. The high-resolution transmission electron microscopy (HRTEM) image revealed that the lattice distance of 0.181 nm corresponds to the (100) lattice face of the hexagonal Cu-MOF.[44,45] Elemental distribution mapping confirmed the uniform carbon, oxygen, and copper distribution of the CMM (Fig. S2b†). Fig. 2a–d illustrates the time-dependent formation process of CMM-70. The formation of the hollow structure is attributed to the Kirkendall effect, whereby the ionic size of the deprotonated ligand anion is larger than that of Cu^{2+}. As a result, the diffusion rate of Cu^{2+} is faster than that of the ligand anions, leading to the formation of a hollow structure. After a reaction time of 2 min, a layer of the solid Cu-MOF shell was observed on the surface of the $Cu(OH)_2$ NWs, resulting in a core–shell structure as shown in Fig. 2b. This MOF shell acts both as a template to maintain the wirelike morphology and a barrier to prevent the inward diffusion of the ligand anions.[41,43]

As the reaction time increased to 5 minutes, voids appeared inside the $Cu(OH)_2$ NWs, with unconverted $Cu(OH)_2$ remaining in the core, leading to a yolk–shell structure, as shown in Fig. 2c. This indicates that the growth of the Cu-MOF shell is dominated by the diffusion of Cu^{2+} from solid $Cu(OH)_2$. After a reaction time of 10 minutes, the voids grew larger and a complete hollow structure with a rough surface composed of Cu-MOF nanoparticles was formed, as shown in Fig. 2d. The dia-

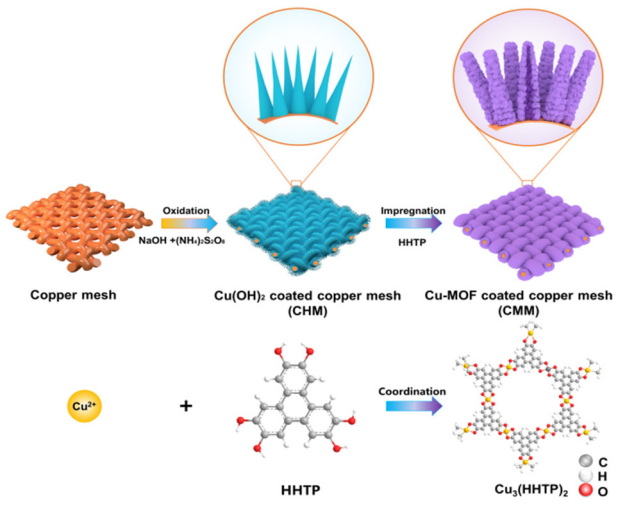

Scheme 1 Schematic illustration of the fabrication process of CMM.

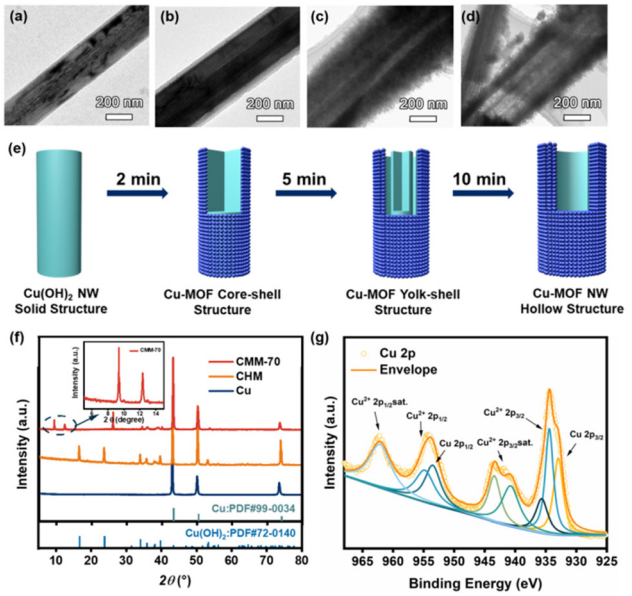

Fig. 2 Phase transformation processes. TEM images showing the evolution of $Cu(OH)_2$ NWs to Cu-MOF hollow structures at (a–d) 0, 2, 5, and 10 min, respectively. (e) Schematic illustration of the formation process of the Cu-MOF NW hollow structure. (f) XRD patterns of pristine copper mesh, CHM, and CMM-70. (g) High-resolution XPS spectra of Cu 2p in CMM-70.

meter of the Cu-MOF hollow NWs was larger than that of the corresponding $Cu(OH)_2$ NWs, possibly due to the outward growth of the porous Cu-MOF shell. Based on the above analysis, the evolution mechanism of CMM-70 is elucidated and presented in Fig. 2e.

X-ray diffraction (XRD) analysis was performed to confirm the crystal structure of the products obtained at different stages of the reaction. As shown in Fig. 2f, all samples exhibited three strong diffraction peaks at $2\theta = 43.3°$, 50.4°, and 74.1°, which can be attributed to the metal copper (JCPDS No. 04-0836).[46] The diffraction pattern of CHM also showed additional characteristic peaks at 16.7°, 23.9°, 34.1°, 35.9°, 38.3°, 39.9°, and 63.5°, which are consistent with the orthorhombic-phase $Cu(OH)_2$ crystal (JCPDS No. 13-0420).[47] In contrast, the diffraction pattern of CMM-70 showed new peaks at 2θ = 9.49, 12.59, and 27.09°, which correspond to the (200), (210), and (002) lattice planes of the $Cu_3(HHTP)_2$ crystals, respectively.[48–50] Furthermore, the diffraction pattern of CMM-70 also exhibited residual diffraction peaks of $Cu(OH)_2$, indicating the incomplete transformation of $Cu(OH)_2$ to the Cu-MOF.

The FT-IR spectra of the pristine copper mesh, CHM, and CMM-70 were analysed, as shown in Fig. S3.† The CHM displayed absorption peaks at 3553, 3291, 942, and 680 cm^{-1}. The bands at 3553 and 3291 cm^{-1} can be attributed to the O–H stretching vibration of $Cu(OH)_2$, while the bands at 942 and 680 cm^{-1} may correspond to the O–H bending vibration of $Cu(OH)_2$.[51] In contrast, the FT-IR spectrum of CMM-70 showed strong characteristic peaks at 1219, 1289, and 1430 cm^{-1}, which can be assigned to the C–H and C=C tensile vibration of the aromatic ring.[52] Additionally, the characteristic peaks in the fingerprint region (800–500 cm^{-1}) may correspond to the C–H bending mode and the ring out-of-plane bending vibrations of the substituted benzene.

To study the chemical state of elements in CMM-70, X-ray photoelectron spectroscopy (XPS) was performed, as shown in Fig. S4† and Fig. 2g. The survey spectrum of CMM-70 revealed the binding energies (BEs) of C 1s, O 1s, and Cu 2p at 282, 539, and 938 eV, respectively (Fig. S4†). Fig. 2g displays the high-resolution XPS spectra of Cu 2p, showing peaks at 934.8 eV and 954.3 eV that correspond to $2p_{3/2}$ and $2p_{1/2}$ of Cu^{2+}, respectively.[50,51] The Cu^{2+} $2p_{3/2}$ signals can be deconvoluted into two peaks (BEs at 934.5 and 935.5 eV), which can be assigned to the coordination of Cu^{2+} with HHTP. Moreover, the BEs at 940.8 eV, 944.6 eV, and 964.4 eV correspond to satellite peaks, indicating the paramagnetic chemical state of Cu^{2+}.[50,51]

3.2. Temperature-dependent growth of the Cu-MOF

The influence of reaction temperature on the morphology of the Cu-MOF is presented in Fig. 3, where the diameter of the products increases gradually with the increase of the reaction temperature. The outward diffusion rate of Cu^{2+} is found to increase with the increase of the reaction temperature, leading to a gradual transformation of the structure from solid NWs to completely hollow NWs and even partial collapse. Although both CMM-70 and CMM-90 displayed well-defined hollow structures, the surface of CMM-90 exhibited partial collapse of the hollow structures, as observed in Fig. S5.†

The XRD measurements shown in Fig. 4 reveal that as the reaction temperature increases from 50 to 90 °C, the peak intensity of $Cu(OH)_2$ gradually decreases, while that of the Cu-MOF increases, indicating a smooth structural transformation. Furthermore, EDX analysis confirms the transformation processes, as shown in Fig. S6,† where the percentage of the C element observed in the Cu-MOF increases with higher reaction temperature.

The N_2 adsorption–desorption results presented in Fig. S7† (with the corresponding data in Table S1†) demonstrate the

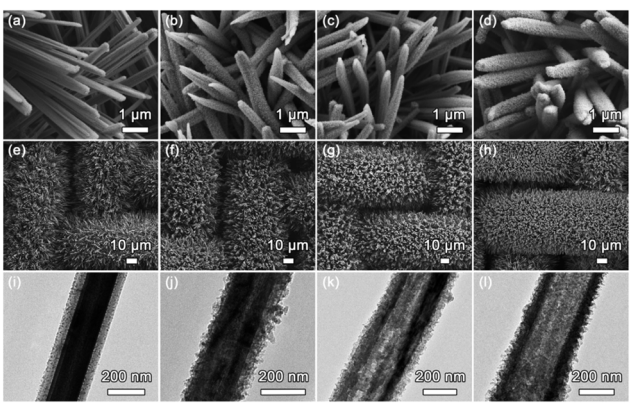

Fig. 3 SEM and TEM images of modified mesh samples obtained at different reaction temperatures: (a, e and i) CMM-30, (b, f and j) CMM-50, (c, g and k) CMM-70, and (d, h and l) CMM-90.

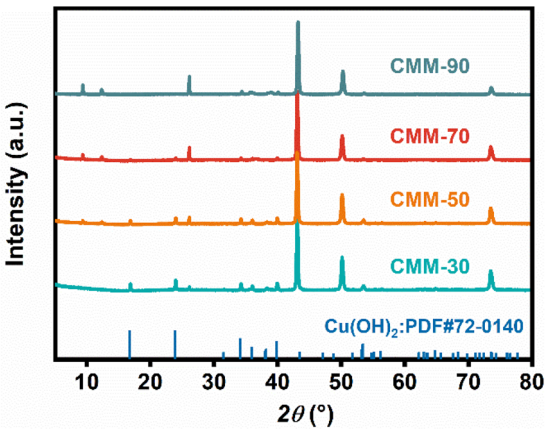

Fig. 4 XRD patterns of modified mesh samples obtained at different reaction temperatures.

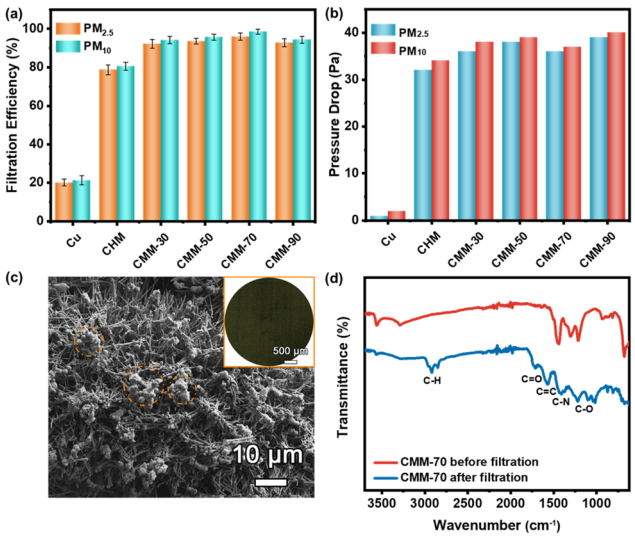

Fig. 5 Air filtration performance. (a) Filtration efficiency and (b) pressure drop against different PM sizes for filters measured using a home-made smoke tester. (c) SEM surface morphology image of the CMM-70 filter after filtration. The orange circles represent the observed PM particles. The inset shows the corresponding photograph of the CMM-70 filter. (d) FT-IR change of CMM-70 before and after filtration.

adsorption isotherm of the CHM and CMM-T filters. The pristine copper mesh displayed almost no specific surface area. However, the specific surface area of the CMM-T showed a progressively increasing trend with the gradual formation of hollow structures. The S_{BET} values of the obtained CMM-30, CMM-50, CMM-70, and CMM-90 filters were 9.19, 15.52, 25.34, and 22.53 $m^2\ g^{-1}$, respectively, all of which were higher than that of CHM (5.13 $m^2\ g^{-1}$). The reduced S_{BET} of CMM-90 was due to the collapse of the hollow structures.

3.3. Filtration performance of the modified copper mesh filters

The filtration properties of the modified mesh filters were evaluated using two filtration tests.

3.3.1. Smoke test *via* a homemade filtration system. The first test was the smoke test, which involved burning cigarettes to generate smoke with PM2.5 and PM10, and was conducted using a homemade filtration system (Fig. S1†).

The filtration efficiency and pressure drop of the pristine copper mesh, CHM, and CMM were evaluated and the results are presented in Fig. 5a, b and Table S2.† The PM2.5 filtration efficiency of the CHM improved significantly from 20.1% of the pristine copper mesh to 78.8% with the growth of $Cu(OH)_2$ NWs. The CMM showed further improvement in PM2.5 filtration efficiency, with the highest filtration efficiency observed in CMM-70 (96.0% for PM2.5 and 98.5% for PM10), which was significantly higher than those of the pristine copper mesh and CHM.

The PM2.5 filtration efficiency of CMM-70 gradually decreased from 96% to 85% after 10 cycles in long-term recycling tests (Fig. S9†). The SEM images revealed a slight collapse (Fig. S10 and S11†). The PMs attached to the surface could be easily washed out with a DI-water/ethanol mixture after PM removal in multiple cycling measurements. The FT-IR spectra of CMM-70 after filtration for 1 h show a significantly increased peak assigned to C–N, C=O, C–O, and C=C bonding, indicating efficient PM2.5 adsorption from the cigarette smoke on CMM-70 (Fig. 5d). The peaks at 1757, 1643, and 1386 cm^{-1} are assigned to C=O, C=C, and C–N. The peak at 1076 cm^{-1} is ascribed to C–O stretching vibrations. The peaks at 875 and 712 cm^{-1} are due to the out-of-plane bending vibration of C–H linked to a benzene ring.

3.3.2. PM filtration measurements *via* a commercial filtration system. In order to investigate filtration in the small-size range, a commercial filtration test was conducted using an aerosol-based NaCl particle generation system (350 g L^{-1} NaCl, a log–normal size distribution). The test particles were characterized as PM0.3, PM0.5, PM1.0, PM2.5, and PM10.

The filtration efficiencies of the pristine copper mesh, CHM, and CMM-70 were investigated and are presented in Fig. S12 and S13.† The copper mesh showed poor filtration performance, while the CHM exhibited good filtration performance for large-size particles (96.9% for PM5.0 and 100% for PM10 at an airflow rate of 12 L min^{-1}). CMM-70 showed excellent filtration performance across all particle size regimes (Table S3†), demonstrating that the Cu-MOF could significantly improve the filtration efficiency, particularly for fine PM particles.

Furthermore, the filtration performance of the CMM filters for fine particles (PM1.0 and PM2.5) at various air flow rates was investigated. The filtration efficiency of all the samples increased and then decreased with an increase in the airflow rate, while the pressure drop tended to increase linearly with the airflow rate (Fig. 6a and b). At an airflow rate of 12 L min^{-1}, all the samples showed the optimal filtration efficiency for PM1.0 and PM2.5. Specifically, CMM-70 exhibited the highest filtration efficiency (93.8% for PM1.0 and 98.1% for PM2.5) compared to the others (PM1.0, 89.6%, 92.4%, and 88% for CMM-30, CMM-50, and CMM-90, and PM2.5, 93.5%, 94.3%, and 92.6% for CMM-30, CMM-50, and CMM-90)

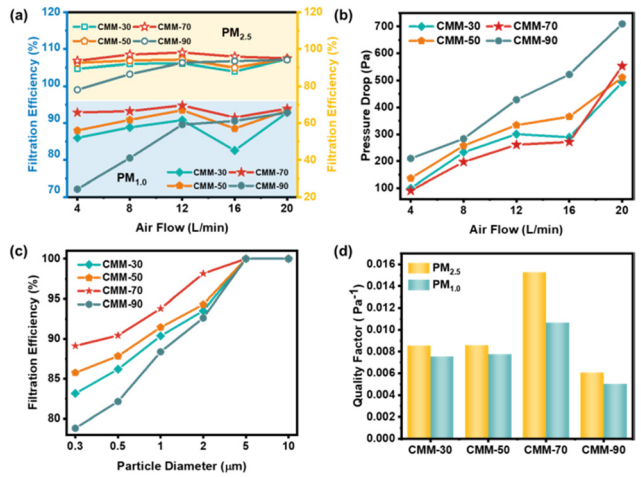

Fig. 6 Filtration performance of CMM-T for $PM_{1.0}$ and $PM_{2.5}$. Relationship between the (a) airflow rate and filtration efficiency, (b) air flow rate and pressure drop, (c) particle size and filtration efficiency, and (d) quality factors for different CMM-T filters.

(Fig. 6a). Compared to the CHM, all CMM-T types demonstrated significantly higher filtration efficiency for small-size particles with the AED being lower than 2.5 μm. It is well-known that passive filtration mechanisms, such as interception, inertial impaction, and diffusion, have less influence on the capture of small-size PM particles.[52–54] Therefore, the electrostatic interaction between the Cu-MOF and PM is likely the dominant factor in the capture enhancement.

It is noteworthy that CMM-70 consistently exhibits the lowest pressure drop across all airflow rates compared to CMM-30 and CMM-50, both of which have solid structures (Fig. 6b). The hollow structure of CMM-70 is believed to be responsible for the increased airflow passage. Although CMM-90 also has a hollow structure, it may experience a collapse of its hollow structure, leading to an increased pressure drop and decreased filtration efficiency.

The filtration efficiency of the CMM-T filters for different sizes of PM particles at an airflow rate of 12 L min^{-1} is depicted in Fig. 6c. All the filters demonstrate excellent filtration performance for large particles (100% for $PM_{5.0}$ and PM_{10}), with the efficiency decreasing as the particle size decreases, reaching its lowest point at 0.3 μm. The filters exhibit different particle capture abilities, with CMM-70 displaying the highest filtration efficiency among all CMM-T filters, particularly for fine particles (89.1% for PM0.3, 90.4% for PM0.5, 93.8% for PM1.0, and 98.1% for PM2.5). Consequently, CMM-70 exhibits the highest quality factor of 0.015 and 0.011 Pa^{-1} for PM2.5 and PM1.0, respectively, at an airflow rate of 12 L min^{-1} (Fig. 6d). It is worth noting that the quality factors obtained using the commercial filtration system are much lower than those obtained using the homemade smoke system, possibly due to the higher airflow rate in commercial filtration system.

In our study, the main air filtration mechanism of the Cu-MOF loaded copper mesh for submicron PMs is attributed to passive trapping including mechanical filtration, such as Brownian diffusion, direct interception, and inertial impaction.[3] However, the filtration efficiency of the mechanical filtration mechanism is limited, especially for fine PM sizes. Therefore, in addition to mechanical filtration, the Cu-MOF loaded copper mesh shows the following additional filtration mechanisms: at first, the surface roughness of the $Cu(OH)_2$ NWs can be improved by *in situ* growth of Cu-MOFs, which produces much more micro/nanoscale pores, and when the airflow containing PMs passes, the PMs are captured in the pores due to the inertial force and insufficient time to bypass the filter along the streamline of the airflow. Secondly, the *in situ* grown Cu-MOFs on 3D $Cu(OH)_2$ NWs could provide a large amount of adsorption sites for fine PMs. The PMs will easily interact with the Cu-MOFs that have positive charges provided by the unbalanced metal ions, thereby enhancing the capacity of the filter to capture PMs. Furthermore, the S_{BET} value of the copper wire can be improved after the *in situ* growth of Cu-MOFs due to their high S_{BET}, enhancing the surface energy of the filter and increasing the deposition probability of fine aerosol particles. Finally, as the density of the Cu-MOFs increases, the airflow is blocked, while the hollow structure could facilitate airflow passage, reducing the pressure drop of the filtration system to some extent.

3.4. Antibacterial properties of mesh filters

The antibacterial efficacy of the filters was evaluated through the plate counting method (Fig. 7a–d). The results showed that all the modified mesh filters, except the pristine copper mesh, exhibited sterilization rates higher than 95% against *E. coli* and *S. aureus*, respectively. The CHM showed higher antibacterial properties against *E. coli* (97.0%) and *S. aureus* (98.6%). CMM-70 demonstrated the highest antibacterial properties

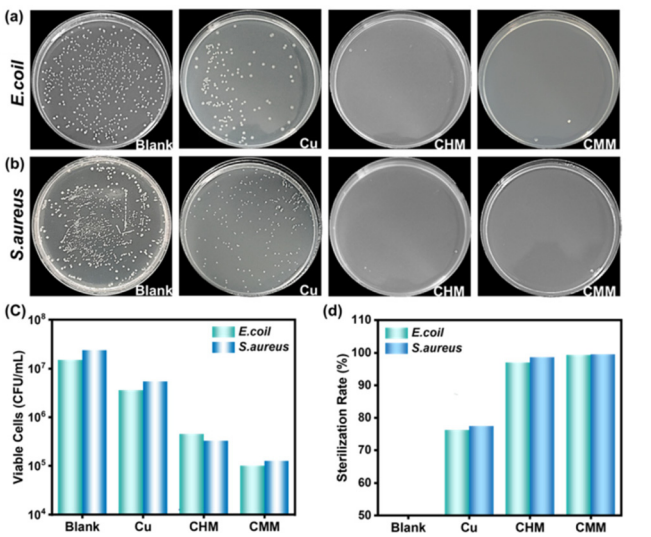

Fig. 7 Antibacterial performance of different mesh filters. Photographs of the (a) *E. coli* and (b) *S. aureus* bacterial colonies formed with different mesh filters. The corresponding (c) viable cells and (d) sterilization rates of different filters on *E. coli* and *S. aureus*.

against *E. coli* (99.3%) and *S. aureus* (99.5%). It is reported that for copper containing surfaces, the antibacterial activity is strongly correlated with the release of copper ions from the surface into the surrounding media. It is generally accepted that copper ions cause a sequence of events that eventually lead to cell death.[55–58] The antibacterial mechanism of the CHM and CMM here could also be attributed to the release of Cu^{2+} ions, which initially adsorb on the cell membrane of bacteria and then infiltrate into the cells through interactions with the hydroxyl groups of peptidoglycans, causing damage to the cell membranes and DNA breakage. The SEM images were further used to observe visually the morphological changes of *E. coli* and *S. aureus* after antibacterial experiments for CMM-70 (Fig. S14†). Both bacteria were damaged by Cu^{2+}-induced antibacterial performance, showing extensive collapse and damage.

4. Conclusions

In this study, a hierarchical 3D Cu-MOF hollow NW coated copper mesh filter was fabricated using a self-sacrificial template method, and its efficient PM-filtering effect was demonstrated. The CMM filter displayed improved filtration performance for PM particles in all size regimes, with particular emphasis on PM2.5 and PM1.0. The MOF-loaded filter also demonstrated excellent antibacterial activity against both *E. coli* and *S. aureus*. Overall, this study offers a straightforward preparation strategy for designing multi-functional MOF-loaded metal filters with high filtration performance across all particle size regimes. These highly efficient and antibacterial air filters are anticipated to have a wide range of applications in energy-efficient metal-based purification/separation devices and indoor air cleaning systems.

Author contributions

Supervision, resources, writing – review, and editing: Tao Wang, Yulong Ying, and Sheng Wang. Methodology, experiments, and data curation: Haiyan Li, Zhiqi Wang, and Lianjun Pan. The manuscript was written through contributions of all authors. All authors have given approval to the final version of the manuscript.

Conflicts of interest

There are no conflicts to declare.

Acknowledgements

We thank the Natural Science Foundation of Zhejiang province (LZ22C100002 and LQ22B010006), and 521 Talent Project of Zhejiang Sci-Tech University for providing financial support. The authors would like to thank Suzhou Huada Instrument Equipment Co., Ltd for the support with PM filtration tests.

References

1 Q. Zhang, X. Jiang, D. Tong, S. J. Davis, H. Zhao, G. Geng, T. Feng, B. Zheng, Z. Lu, D. G. Streets, R. Ni, M. Brauer, A. V. Donkelaar, R. V. Martin, H. Huo, Z. Liu, D. Pan, H. Kan, Y. Yan, J. Lin, K. He and D. Guan, *Nature*, 2017, **543**, 705–709.
2 S. Zhang, H. Liu, N. Tang, S. Zhou, J. Yu and B. Ding, Spider-web-inspired $PM_{0.3}$ filters based on self-sustained electrostatic nanostructured networks, *Adv. Mater.*, 2020, **32**, 2002361.
3 Z. Li, Q. Wen and R. Zhang, Sources, health effects and control strategies of indoor fine particulate matter ($PM_{2.5}$): A review, *Sci. Total Environ.*, 2017, **586**, 610–622.
4 J. O. Anderson, J. G. Thundiyil and A. Stolbach, Clearing the Air: A review of the effects of particulate matter air pollution on human health, *J. Med. Toxicol.*, 2020, **8**, 166–175.
5 A. Nel, Air pollution-related illnesses: Effects of particles, *Science*, 2005, **308**, 804–806.
6 S. Han, J. Kim and S. H. Ko, Advances in air filtration technologies: structure-based and interaction-based approaches, *Mater. Today Adv.*, 2021, **9**, 100134.
7 J. Xiao, J. Liang, C. Zhang, Y. Tao, G. W. Ling and Q. H. Yang, Advanced materials for capturing particulate matter: Progress and perspectives, *Small Methods*, 2018, **2**, 1800012.
8 S. Han, J. Kim and S. H. Ko, Advances in air filtration technologies: structure-based and interaction-based approaches, *Mater. Today Adv.*, 2021, **9**, 100134.
9 Kenry and C. T. Lim, Nanofiber technology: current status and emerging developments, *Prog. Polym. Sci.*, 2017, **70**, 1–17.
10 T. Xia and C. Chen, Evolution of pressure drop across electrospun nanofiber filters clogged by solid particles and its influence on indoor particulate air pollution control, *J. Hazard. Mater.*, 2021, **402**, 123479.
11 T. Xia, Y. Bian, S. Shi, L. Zhang and C. Chen, Influence of nanofiber window screens on indoor $PM_{2.5}$ of outdoor origin and ventilation rate: An experimental and modeling study, *Build. Simul.*, 2020, **13**, 873–886.
12 S. Mohankumar and P. Senthilkumar, Particulate matter formation and its control methodologies for diesel engine: A comprehensive review, *Renewable Sustainable Energy Rev.*, 2017, **80**, 1227–1238.
13 C. Liu, P.-C. Hsu, H.-W. Lee, M. Ye, G. Zheng, N. Liu, W. Li and Y. Cui, Transparent air filter for high-efficiency $PM_{2.5}$ capture, *Nat. Commun.*, 2015, **6**, 6205.
14 X. Ma, Y. Chai, P. Li and B. Wang, Metal–organic framework films and their potential applications in environmental pollution control, *Acc. Chem. Res.*, 2019, **52**, 1461–14705.

15 J. Xu, C. Liu, P. C. Hsu, K. Liu, R. Zhang, Y. Liu and Y. Cui, Roll-to-roll transfer of electrospun nanofiber film for high-efficiency transparent air filter, *Nano Lett.*, 2016, **16**, 1270–1275.

16 S. Wang, X. L. Zhao, X. Yin, J. Y. Yu and B. Ding, Electret polyvinylidene fluoride nanofibers hybridized by polytetrafluoroethylene nanoparticles for high-efficiency air filtration, *ACS Appl. Mater. Interfaces*, 2016, **8**, 23985–23994.

17 G. Q. Gu, C. B. Han, C. X. Lu, C. He, T. Jiang, Z. L. Gao, C. J. Li and Z. L. Wang, Triboelectric nanogenerator enhanced nanofiber air filters for efficient particulate matter removal, *ACS Nano*, 2017, **11**, 6211–6217.

18 T. Kitao, Y. Zhang, S. Kitagawa, B. Wang and T. Uemura, Hybridization of MOFs and polymers, *Chem. Soc. Rev.*, 2017, **46**, 3108–3133.

19 Y. Qian, F. Zhang and H. Pang, A review of MOFs and their composites-based photocatalysts: Synthesis and applications, *Adv. Funct. Mater.*, 2021, **31**, 2104231.

20 L. Ji, H. Zheng, Y. Wei, S. Gong, T. Wang, S. Wang and Z. Chen, Temperature-controlled fabrication of Co-Fe-based nanoframes for efficient oxygen evolution, *Sci. China Mater.*, 2022, **65**, 431–441.

21 H. Huang, J. Li, M. Yuan, H. Yang, Y. Zhao, Y. Ying and S. Wang, Large-scale self-assembly of MOFs colloidosomes for bubble-propelled micromotors and stirring-free environmental remediation, *Angew. Chem., Int. Ed.*, 2022, **61**, e202211163.

22 Y. Zhang, S. Yuan, X. Feng, H. Li, J. Zhou and B. Wang, Preparation of nanofibrous metal–organic framework filters for efficient air pollution control, *J. Am. Chem. Soc.*, 2016, **138**, 5785–5788.

23 X. Ji, J. Huang, L. Teng, S. Li, X. Li, W. Cai, Z. Chen and Y. Lai, Advances in particulate matter filtration: Materials, performance, and application, *Green Energy Environ.*, 2022, DOI: **10.1016/j.gee.2022.03.012**.

24 D. K. Yoo, H. C. Woo and S. H. Jhung, Removal of particulate matter with metal–organic framework-incorporated materials, *Coord. Chem. Rev.*, 2020, **422**, 213477.

25 Z. Su, M. Zhang, Z. Lu, S. Song, Y. Zhao and Y. Hao, Functionalisation of cellulose fiber by in situ growth of zeolitic imidazolate framework-8 (Zif-8) nanocrystals for preparing a cellulose-based air filter with gas adsorption ability, *Cellulose*, 2018, **25**, 1997–2008.

26 S. Ma, M. Zhang, J. Nie, J. Tan, B. Yang and S. Song, Design of double-component metal-organic framework air filters with $PM_{2.5}$ capture, gas adsorption and antibacterial capacities, *Carbohydr. Polym.*, 2019, **203**, 415–422.

27 Z. Li, G. Zhou, H. Dai, M. Yang, Y. Fu, Y. Ying and Y. Li, Biomineralization-mimetic preparation of hybrid membranes with ultra-high loading of pristine metal–organic frameworks grown on silk nanofibers for hazard collection in water, *J. Mater. Chem. A*, 2018, **6**, 3402–3413.

28 Y. Chen, S. Zhang, S. Cao, S. Li, F. Chen, S. Yuan, C. Xu, J. Zhou, X. Feng, X. Ma and B. Wang, Roll-to-roll production of metal-organic framework coatings for particulate matter removal, *Adv. Mater.*, 2017, **29**, 1606221.

29 Y.-S. Li, F.-Y. Liang, H. Bux, A. Feldhoff, W.-S. Yang and J. Caro, Molecular sieve membrane: supported metal-organic framework with high hydrogen selectivity, *Angew. Chem., Int. Ed.*, 2010, **49**, 548–551.

30 A. Huang, W. Dou and J. Caro, Steam-stable zeolitic imidazolate framework ZIF-90 membrane with hydrogen selectivity through covalent functionalization, *J. Am. Chem. Soc.*, 2010, **132**, 15562–15564.

31 Y. Zhang, Y. Zhang, X. Wang, J. Yu and B. Ding, Ultrahigh metal–organic framework loading and flexible nanofibrous membranes for efficient CO_2 capture with long-term, ultrastable recyclability, *ACS Appl. Mater. Interfaces*, 2018, **10**, 34802–34810.

32 M. Lee, G. P. Ojha, H. J. Oh, T. Kim and H. Y. Kim, Copper// terbium dual metal organic frameworks incorporated side-by-side electrospun nanofibrous membrane: A novel tactics for an efficient adsorption of particulate matter and luminescence property, *J. Colloid Interface Sci.*, 2020, **578**, 155–163.

33 D. Wang, B. Zhu, X. He, Z. Zhu, G. Hutchins, P. Xu and W. N. Wang, Iron oxide nanowires based filter for inactivation of airborne bacteria, *Environ. Sci.: Nano*, 2018, **5**, 1096–1106.

34 S. J. Dunnett and C. F. Clement, Numerical investigation into the loading behaviour of filters operating in the diffusional and interception deposition regimes, *J. Aerosol Sci.*, 2012, **53**, 85–99.

35 S. I. Choi, J. Feng, S. B. Kim and Y. M. Jo, Magnetization of metal mesh for fine dust capture, *Aerosol Air Qual. Res.*, 2018, **18**, 1932–1943.

36 K. Yang, Z. Yu, C. Yu, H. Chen and F. Pan, An electrically renewable air filter with integrated 3D nanowire networks, *Adv. Mater. Technol.*, 2019, **4**, 1900101.

37 Z. Wang, T. Wang, Z. Zhang, L. Ji, L. Pan and S. Wang, ZIF-67 grown on a fibrous substrate via a sacrificial template method for efficient $PM_{2.5}$ capture and enhanced antibacterial performance, *Sep. Purif. Technol.*, 2022, **280**, 119814.

38 J. Liu, L. Wang, N. Wang, F. Guo, L. Hou, Y. Chen, J. Liu, Y. Zhao and L. Jiang, A robust $Cu(OH)_2$ nanoneedles mesh with tunable wettability for nonaqueous multiphase liquid separation, *Small*, 2017, **13**, 1600499.

39 F. Chen, J. Ma, Y. Zhu, X. Li, H. Yu and Y. Sun, Biodegradation Performance and anti-fouling mechanism of an ICME/electro-biocarriers-MBR system in livestock wastewater (antibiotic-containing) treatment, *J. Hazard. Mater.*, 2022, **426**, 128064.

40 S. Zhu, Y. Chen, M. A. Khan, H. Xu, F. Wang and M. Xia, In-depth study of heavy metal removal by an etidronic acid-functionalized layered double hydroxide, *ACS Appl. Mater. Interfaces*, 2022, **14**, 7450–7463.

41 H. J. Fan, M. Knez, R. Scholz, D. Hesse, K. Nielsch, M. Zacharias and U. Gösele, Influence of surface diffusion on the formation of hollow nanostructures induced by the Kirkendall effect: The basic concept, *Nano Lett.*, 2007, **7**, 993–997.

42 X. Wang, J. Feng, Y. Bai, Q. Zhang and Y. Yin, Synthesis, properties, and applications of hollow micro-/nanostructures, *Chem. Rev.*, 2016, **116**, 10983–11060.
43 X. Zhang, C. Y. Chuah, P. Dong, Y. H. Cha, T. H. Bae and M. K. Song, Hierarchically porous Co-MOF-74 hollow nanorods for enhanced dynamic CO_2 separation, *ACS Appl. Mater. Interfaces*, 2018, **10**, 43316–43322.
44 S. Gu, Z. Bai, S. Majumder, B. Huang and G. Chen, Conductive metal–organic framework with redox metal center as cathode for high rate performance lithium ion battery, *J. Power Sources*, 2019, **429**, 22–29.
45 R. Li, S. Li, Q. Zhang, Y. Li and H. Wang, Layer-by-layer assembled triphenylene-based MOFs films for electrochromic electrode, *Inorg. Chem. Commun.*, 2021, **123**, 108354.
46 Y. Yin, L. Zhu, T. Guo, X. Qiao, S. Gan, X. Chang, X. Li, F. Xia and Q. Xue, Microphone-like Cu-CAT-1 hierarchical structures with ultra-low oil adhesion for highly efficient oil/water separation, *Sep. Purif. Technol.*, 2020, **241**, 116688.
47 G. N. Ren, Y. M. Song, X. M. Li, Y. L. Zhou, Z. Z. Zhang and X. T. Zhu, A superhydrophobic copper mesh as an advanced platform for oil-water separation, *Appl. Surf. Sci.*, 2018, **428**, 520–525.
48 Q. Ma, P. Yin, M. Zhao, Z. Luo, Y. Huang, Q. He, Y. Yu, Z. Liu, Z. Hu, B. Chen and H. Zhang, MOF-based hierarchical structures for solar-thermal clean water production, *Adv. Mater.*, 2019, **31**, 1808249.
49 M. S. Yao, X. J. Lv, Z. H. Fu, W. H. Li, W. H. Deng, G. D. Wu and G. Xu, Layer-by-Layer Assembled Conductive Metal-Organic Framework Nanofilms for Room-Temperature Chemiresistive Sensing, *Angew. Chem.*, 2017, **129**, 16510–16514.
50 M. Hmadeh, Z. Lu, Z. Liu, F. Gándara, H. Furukawa, S. Wan, V. Augustyn, R. Chang, L. Liao, F. Zhou, E. Perre, V. Ozolins, K. Suenaga, X. Duan, B. Dunn, Y. Yamamto, O. Terasaki and O. M. Yaghi, New porous crystals of extended metal-catecholates, *Chem. Mater.*, 2012, **24**, 3511–3513.
51 Z. Shami, A. Gharloghi and S. M. Amininasab, Multifunctional pH-switched superwetting copolymer nanotextile: Surface engineered toward on-demand light oil-water separation on super-hydrophilic-underwater low-adhesive superoleophobic nonwoven mesh, *ACS Sustainable Chem. Eng.*, 2019, **7**, 8917–8930.
52 S. Hwang, W. S. Chi, S. J. Lee, S. H. Im, J. H. Kim and J. Kim, Hollow ZIF-8 nanoparticles improve the permeability of mixed matrix membranes for CO_2/CH_4 gas separation, *J. Membr. Sci.*, 2015, **480**, 11–19.
53 Y. Bian, Z. Niu, S. Wang, Y. Pan, L. Zhang and C. Chen, Removal of size-dependent submicron particles using metal–organic framework-based nanofiber air filters, *ACS Appl. Mater. Interfaces*, 2022, **14**, 23570–23576.
54 Y. V. Kaneti, J. Tang, R. R. Salunkhe, X. Jiang, A. Yu, K. C. Wu and Y. Yamauchi, Nanoarchitectured design of porous materials and nanocomposites from metal-organic frameworks, *Adv. Mater.*, 2017, **29**, 1604898.
55 H. N. Rubin, B. H. Neufeld and M. M. Reynolds, Surface-anchored metal–organic framework–cotton material for tunable antibacterial copper delivery, *ACS Appl. Mater. Interfaces*, 2018, **10**, 15189–15199.
56 J. Xiao, Y. Zhu, S. Huddleston, P. Li, B. Xiao, O. K. Farha and G. A. Ameer, Copper metal–organic framework nanoparticles stabilized with folic acid improve wound healing in diabetes, *ACS Nano*, 2018, **12**, 1023–1032.
57 Z. Chen, J. Wang, M. Hao, Y. Xie, X. Liu, H. Yang, G. I. N. Waterhouse, X. Wang and S. Ma, Tuning excited state electronic structure and charge transport in covalent organic frameworks for enhanced photocatalytic performance, *Nat. Commun.*, 2023, **14**, 1106.
58 M. Hao, Y. Xie, X. Liu, Z. Chen, H. Yang, G. I. N. Waterhouse, S. Ma and X. Wang, *JACS Au*, 2023, **3**, 239–251.